The Astrophysical Journal, 860:87 (7pp), 2018 June 20 https://doi.org/10.3847/1538-4357/aac49a
© 2018. The American Astronomical Society. All rights reserved.

The Discovery of a New Massive Molecular Gas Component Associated with the Submillimeter Galaxy SMM J02399-0136

David T. Frayer[1], Ronald J. Maddalena[1], R. J. Ivison[2,3], Ian Smail[4], Andrew W. Blain[5], and Paul Vanden Bout[6]
[1] Green Bank Observatory, P.O. Box 2, Green Bank, WV 24944, USA; dfrayer@nrao.edu
[2] European Southern Observatory, Karl-Schwarzschild-Straße 2, D-85748 Garching, Germany
[3] Institute for Astronomy, University of Edinburgh, Royal Observatory, Blackford Hill, Edinburgh EH9 3HJ, UK
[4] Centre for Extragalactic Astronomy, Department of Physics, Durham University, South Road, Durham DH1 3LE, UK
[5] University of Leicester, Physics & Astronomy, University Road, Leicester, LE1 7RH, UK
[6] National Radio Astronomy Observatory, 520 Edgemont Road, Charlottesville, VA 22903, USA
Received 2018 April 2; revised 2018 May 9; accepted 2018 May 11; published 2018 June 15

Abstract

We present CO(1–0), CO(3–2), and CO(7–6) observations using the Green Bank Telescope (GBT) and the Atacama Large Millimeter Array (ALMA) of the $z = 2.8$ submillimeter galaxy SMM J02399−0136. This was the first submillimeter-selected galaxy discovered and remains an archetype of the class, comprising a merger of several massive and active components, including a quasar-luminosity AGN and a highly obscured, gas-rich starburst spread over a ∼25 kpc extent. The GBT CO(1–0) line profile is comprised of two distinct velocity components separated by about 600 km s^{-1} and suggests the presence of a new component of molecular gas that had not been previously identified. The CO(3–2) observations with ALMA show that this new component, designated W1, is associated with a large extended structure stretching 13 kpc westward from the AGN. W1 is not detected in the ALMA CO(7–6) data, implying that this gas has much lower CO excitation than the central starburst regions, which are bright in CO(7–6). The molecular gas mass of W1 is about 30% of the total molecular gas mass in the system, depending on the CO-to-H_2 conversion factor. W1 is arguably a merger remnant; alternatively, it could be a massive molecular outflow associated with the AGN, or perhaps inflowing metal-enriched molecular gas fueling the ongoing activity.

Key words: galaxies: active – galaxies: evolution – galaxies: high-redshift – galaxies: individual (SMM J02399-0136) – galaxies: starburst

1. Introduction

More than 20 years ago, the first submillimeter-selected galaxies (SMGs) were discovered (Smail et al. 1997; Barger et al. 1998; Hughes et al. 1998). The very first SMG detected, SMM J02399−0136 (SMM02399), was uncovered during the initial surveys of massive cluster lenses that were used to magnify previously unknown background SMGs (Smail et al. 1997). SMM02399 was also the first SMG with a redshift (Ivison et al. 1998) and the first SMG detected in CO (Frayer et al. 1998). The discovery of SMGs revolutionized our understanding of the high-redshift universe by uncovering a new population of starburst galaxies that are extremely luminous in the infrared (Blain et al. 2002; Casey et al. 2014).

Over the last two decades, SMM02399 has been studied in great detail, and the source has profoundly influenced our understanding of SMGs in general (Ivison et al. 1998, 2010; Bautz et al. 2000; Vernet & Cimatti 2001; Genzel et al. 2003; Lutz et al. 2005; Valiante et al. 2007; Ferkinhoff et al. 2010, 2011, 2015; Walter et al. 2011; Thomson et al. 2012; Aguirre et al. 2013). SMM02399 is comprised of multiple components, including a bright QSO (L1; Ivison et al. 1998; Vernet & Cimatti 2001), which appears to be merging with or is associated with a nearby extremely red starburst region (L2SW, Ivison et al. 2010; L1sb, Aguirre et al. 2013). The optical components of SMM02399 are shown in Figure 1.

Since SMM02399 is weakly lensed by a foreground cluster (Abell 370 at $z = 0.37$), differential lensing across the source is not expected to be significant. Therefore, one can easily interpret line ratios and the relative strengths of emission from different regions within SMM02399, while also benefiting from the boost in brightness and resolution provided by the foreground lens. For the intrinsic values computed within this paper, we adopt a magnification factor of 2.38 ± 0.08 (Ivison et al. 2010).

The nature of the molecular gas in this system is still unclear. Based on CO(3–2) imaging with the Plateau de Bure Interferometer, Genzel et al. (2003) argued that the molecular gas lies in a rapidly rotating disk around the QSO, but more recent CO(1–0) observations with the Karl G. Jansky Very Large Array (VLA) suggest that the bulk of the molecular gas is associated with the extremely red starburst region L2SW (Ivison et al. 2010; Thomson et al. 2012). Given the multiple optical components and that the system is associated with a large diffuse Lyα halo spread over at least 13″ (Vernet & Cimatti 2001), it is possible that significant molecular emission may have been missed in the previous interferometric studies. In order to test this idea, we have carried out CO(1–0) observations with the Robert C. Byrd Green Bank Telescope (GBT). We also present results based on Atacama Large Millimeter Array (ALMA) CO(3–2) and CO(7–6) observations that are helpful in the interpretation of the GBT CO(1–0) data. Additional results from the ALMA data for SMM02399 will be discussed in a future paper.

A cosmology of $H_0 = 70$ km s^{-1} Mpc^{-1}, $\Omega_M = 0.3$, and $\Omega_\Lambda = 0.7$ is assumed throughout this paper. At the redshift of $z = 2.808$ for SMM02399, this corresponds to an image plane angular scale of 7.85 kpc arcsec^{-1} and a luminosity distance of 23,470 Mpc.

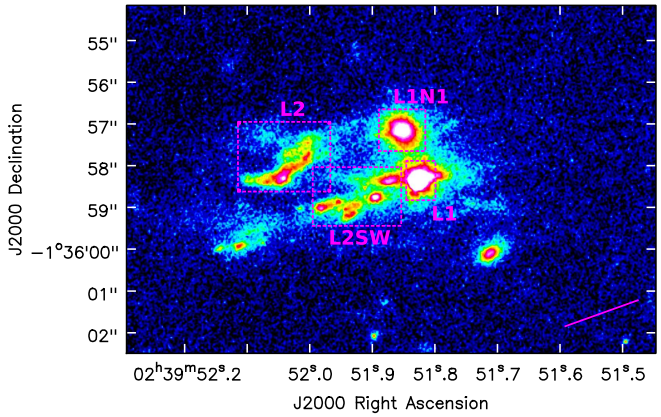

Figure 1. *HST* F814W (rest-frame 214 nm) image of SMM02399 from the Frontier Fields archival data of the cluster Abell 370 (Lotz et al. 2017). The components are labeled with dotted boxes as identified by Ivison et al. (2010). The source is magnified by a factor of 2.38, and the line segment to the lower right indicates the lensing shear direction (Ivison et al. 2010).

2. Observations

2.1. GBT Observations

The GBT observations of SMM02399 were carried out in 2016 April and 2017 October. In total, we collected 10.1 hr of on-source integration time taken over seven observing sessions (Table 1). The observations targeted the CO(1–0) line at 30.2708 GHz, corresponding to a redshift of $z = 2.808$ (Frayer et al. 1998) using the Versatile GBT Astronomical Spectrometer (VEGAS) with a bandwidth of 1080 MHz and a raw spectral resolution of 66 kHz (0.65 km s^{-1}). We pointed the telescope at the millimeter continuum centroid of (J2000) $02^h39^m51^s.87$, $-01°35'58''.8$ (Genzel et al. 2003).

The observations were taken using subreflector beam-switching ("SubBeamNod"), with a 6-second switching period between the two beams of the Ka-band receiver that are separated by 78″ on the sky. The beam size at the observed frequency is about 25″, which is sufficient to cover all of the source components, including the large diffuse Lyα cloud.

The observations of broad, weak lines for single-dish telescopes are limited by baseline stability, even for the GBT whose off-axis optics avoids the strong standing waves from support structures that often plague symmetric antennae. The observing strategy was optimized to minimize baseline issues and to produce an accurate CO(1–0) profile. Two spectral windows were offset by 150 MHz to provide a check on the baseline performance of the system downstream of the receiver. Alternating SubBeamNod observations between the target and blank sky were taken every 2–3 minutes to remove the residual baseline structure. We collected SubBeamNod scans of the bright nearby pointing source (J0217+0144) before and after the pointing and focus scans to track the losses due to pointing and focus drifts.

The absolute flux density scale was derived from observations of 3C48. Based on the VLA calibration study of Perley & Butler (2013), we adopt a flux density of 0.91 Jy for 3C48. The uncertainty in converting the observed GBT antenna temperature scale into flux density is estimated to be 12%. This uncertainty includes the uncertainty of the VLA calibration scale, measurement errors, the uncertainty for the atmosphere correction, and the uncertainty associated with the pointing and focus drifts.

Table 1
GBT Observations

Date (UT)	GBT Project	Session	Zenith Opacity	On-Source Time[a](s)
2016 Apr 05	16A055	02	0.032	2815
2016 Apr 13	16A055	03	0.039	4944
2016 Apr 23	16A055	04	0.057	1824
2016 Apr 24	16A055	05	0.043	9458
2017 Oct 07	17B192	01	0.071	5056
2017 Oct 21	17B192	02	0.052	6870
2017 Oct 27	17B192	03	0.044	5313

Note.
[a] The on-source time does not include the reference blank-sky scans or data flagged when the subreflector was in motion.

Table 2
ALMA Observations

Date (UT)	Number Antenna	Baselines (m)	CO Transition	On-Source Time (s)
2014 Jun 13	34	19–650	CO(7–6)	816
2015 Jul 01	34	43–1574	CO(3–2)	1239
2015 Sep 05	36	15–1574	CO(3–2)	2328
2016 Aug 12	36	15–1462	CO(3–2)	2328

2.2. GBT Data Reduction

The GBT spectral-line data were reduced using GBTIDL (Marganian et al. 2006). After the standard reduction of the SubBeamNod scans, there are significant residual baseline issues in the data on several different frequency and timescales related to multiple instrumental effects, including the different optical paths of the two subreflector positions, and the receiver itself, as well as issues with thermal stability within the equipment room, which contains several key analog components and VEGAS.

To mitigate the residual baseline structures, the blank-sky scans taken immediately before and after each target scan were averaged and used to derive a polynomial baseline that was removed from each target scan before co-addition. This method worked well for most of the data, but scans still showing residual baseline structures with noise levels higher than expected were deleted before co-addition. The data for each of the two beams and each of the two spectral windows were processed independently before combining. The resulting final spectrum shows a broad component of molecular gas (component B) and a narrow component (component A) centered at 330 km s^{-1} (Figure 2). The GBT data were reduced using various methods to verify the results. The shape of the CO(1–0) profile was confirmed using subsets of the data for the different beams and different spectral windows.

2.3. ALMA Observations

The ALMA CO(3–2) and CO(7–6) observations of SMM02399 were carried out in four observing sessions taken in Cycle-2 and Cycle-3 (Table 2). The raw ALMA visibilities were calibrated using CASA (McMullin et al. 2007) by the North American ALMA Science Center. The data were imaged using natural weighting to maximize the signal-to-noise ratio. The spatial resolutions of the CO(3–2) and CO(7–6) data are $0''.7 \times 0''.6$ and $0''.6 \times 0''.5$, respectively. The data were

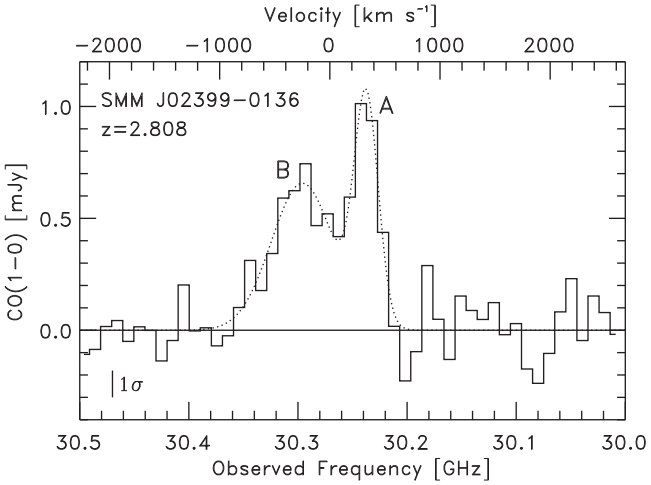

Figure 2. GBT CO(1–0) spectrum of SMM02399. The raw data have been smoothed to a channel resolution of 100 km s^{-1}. The 1σ noise of 0.12 mJy per channel is shown in the lower left. The dotted line shows the fit of a double Gaussian profile to the data. The velocity scale is based on a redshift of $z = 2.808$.

smoothed to produce image cubes with 100 km s^{-1} and 300 km s^{-1} velocity resolutions for analysis and comparison with the GBT CO(1–0) data. The noise levels per 100 km s^{-1} channel are 0.12 mJy and 0.33 mJy for the CO(3–2) and CO (7–6) data, respectively.

3. Results

3.1. GBT CO(1–0) Results

The GBT CO(1–0) profile is consistent with two Gaussian components: (A) a narrow component at 330 km s^{-1} and (B) a broad component centered at −250 km s^{-1} (Table 3). Previously published CO profiles of SMM02399 (Frayer et al. 1998; Genzel et al. 2003; Thomson et al. 2012) also showed a double peak profile. However, for each of these interferometric studies, the strength of the peak at negative velocities was larger or similar to the strength of the peak observed at positive velocities. The GBT CO(1–0) profile shows a significant excess for the positive velocity component (A) in comparison to the VLA (Figure 3), which highlights the importance of the single-dish observations. The narrow component (A) accounts for 38% ± 7% of the total CO(1–0) line flux.

Although the GBT profile shows excess emission for component (A), the integrated CO(1–0) line flux from the GBT is similar to previous results from the VLA within the uncertainties. The integrated GBT CO(1–0) line flux is 0.73 ± 0.10 Jy km s^{-1}. The uncertainty includes the 12% calibration uncertainty combined in quadrature with the measurement error. In comparison with VLA observations, Thomson et al. (2012) measured a CO(1–0) line flux of 0.60 ± 0.12 Jy km s^{-1} and Ivison et al. (2010) derived a value of 0.70 ± 0.18 Jy km s^{-1}. Summing over the channels in the VLA CO(1–0) profile shown in Thomson et al. (2012) would suggest an integrated line flux of only 0.47 Jy km s^{-1}, which is less than their tabulated value of 0.60 Jy km s^{-1}. The higher value is likely more appropriate based on the Ivison et al. (2010) results. We scaled the VLA CO(1–0) spectrum from Thomson et al. (2012) to match their tabulated line flux of 0.60 Jy km s^{-1} in Figure 3. With this scaling, the strength of

Table 3
CO(1–0) Measurements for Velocity Components

	Peak (mJy)	FWHM (km s^{-1})	Frequency (MHz)	Velocity[a] (km s^{-1})
(A)	1.00 ± 0.11	260 ± 35	30237.4 ± 1.4	330 ± 15
(B)	0.66 ± 0.07	660 ± 100	30295.9 ± 3.5	−250 ± 35

Notes. Properties derived from fitting a double Gaussian to the CO(1–0) line profile.
[a] The velocity is with respect to a redshift of $z = 2.808$.

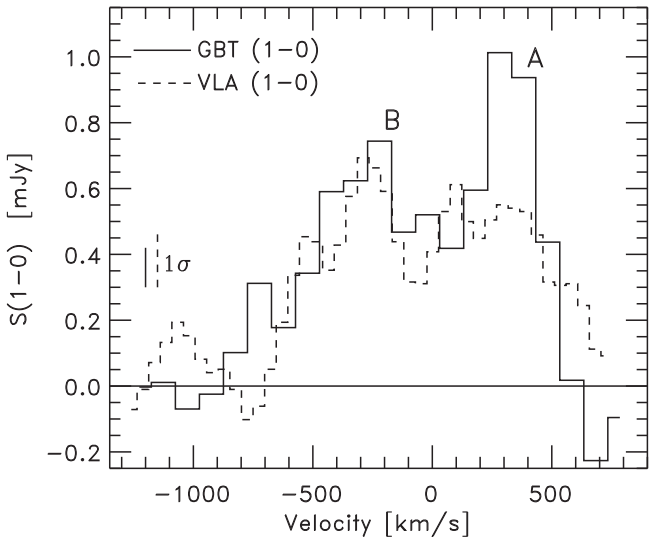

Figure 3. GBT CO(1–0) spectrum compared with the published VLA CO(1–0) spectrum (Thomson et al. 2012). The VLA spectrum has been scaled by 1.3 to match the total integrated line flux reported by the authors. The GBT spectrum shows excess emission for component (A). The 1σ noise levels are shown to the left.

velocity component (B) is consistent between the GBT and the VLA.

Based on the CO(1–0) line flux and correcting for lensing, the intrinsic CO(1–0) line luminosity for SMM02399 is $L'(\mathrm{CO}) = (1.1 \pm 0.2) \times 10^{11}$ K km s^{-1} pc^2. Depending on the CO-to-H_2 conversion factor (α_{CO}), the derived CO luminosity corresponds to a molecular gas mass of $(1.1 \pm 0.2) \times 10^{11} \alpha\, M_\odot$, where α is a unit-less scalar representing the α_{CO} value.

3.2. ALMA CO Results

The ALMA CO(7–6) observations revealed emission from the two central optical components L2SW and L1. The CO (7–6) velocity profiles from both of these components are similar to velocity component (B) of the CO(1–0) profile (Figure 4). There is no evidence of any CO(7–6) emission associated with velocity component (A). This is an important result that is fundamental to our understanding of the source. Previously, it has been speculated that the two peaks of the CO profile may arise from the two optical components L1 and L2 of the merger system (e.g., Frayer et al. 1998) or represent a double-horn profile associated with a molecular gas disk rotating around L1 (Genzel et al. 2003). The ALMA data rules out both of these interpretations. Based on the CO(7–6) data, the AGN (L1) and the red starburst region (L2SW) are at similar systemic velocities corresponding to component (B) of the CO(1–0) profile, and the narrow component (A) represents

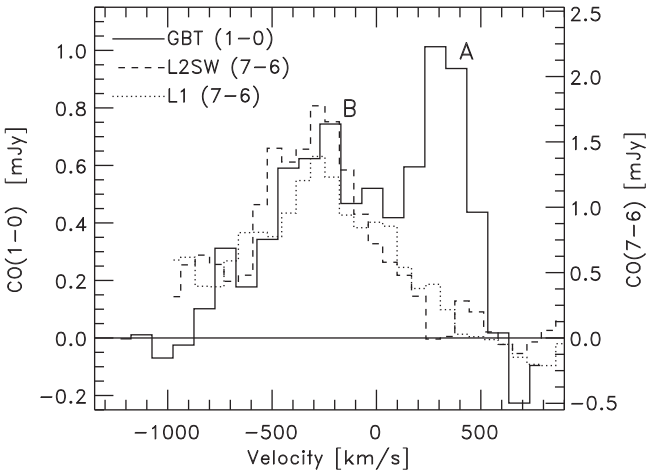

Figure 4. ALMA CO(7–6) spectrum for L2SW and L1, shown as dashed and dotted lines, respectively, compared to the GBT CO(1–0) spectrum. The CO (7–6) emission for both optical components L2SW and L1 is only associated with component (B) of the CO(1–0) profile and is not detected for component (A). The CO(7–6) profiles at velocities less than $-700\,\mathrm{km\,s^{-1}}$ are affected by [C I] emission.

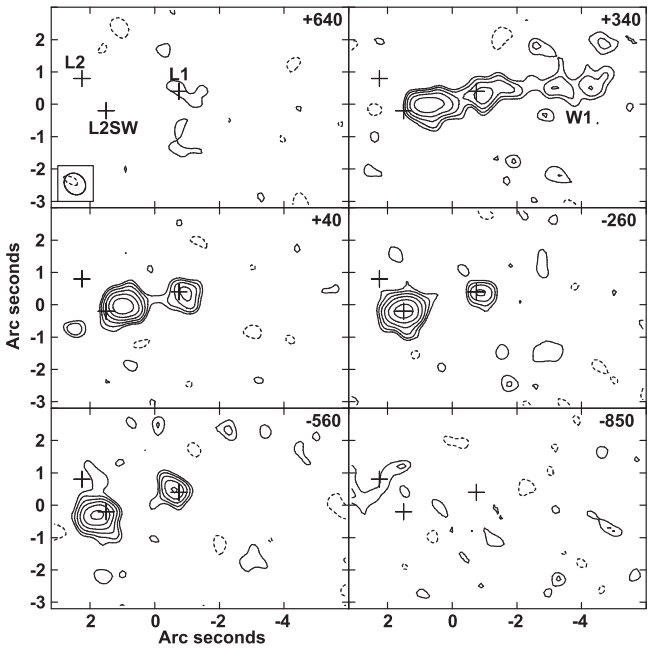

Figure 5. ALMA CO(3–2) channel maps smoothed over $300\,\mathrm{km\,s^{-1}}$. The channel velocity in $\mathrm{km\,s^{-1}}$ with respect to $z = 2.808$ is shown in the upper right of each panel. The crosses mark the positions of the optical components L1, L2, and L2SW and are labeled in the first panel. The new extended western component is labeled W1. The 1σ noise level is $0.02\,\mathrm{Jy\,km\,s^{-1}}$, and the contours start at 2σ and are incremented by $2^{0.5}$ (-2, 2, 2.83, 4, 5.66, 8, 11.3σ). The beam ($0\farcs72 \times 0\farcs61$) is shown in the lower left of the first panel.

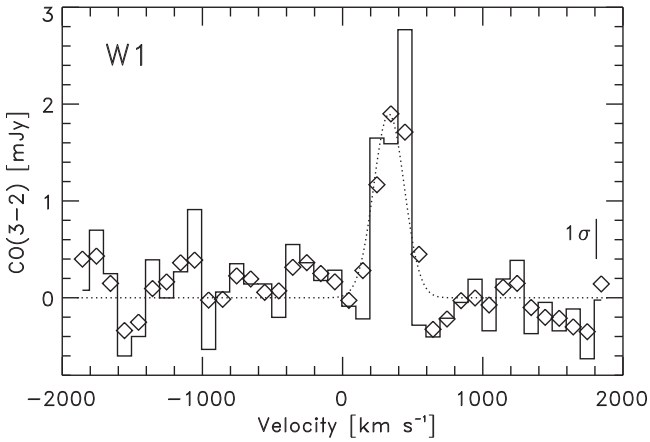

Figure 6. The ALMA CO(3–2) spectrum for the new W1 component of molecular gas. The solid line shows the spectrum with $100\,\mathrm{km\,s^{-1}}$ channels, and the 1σ error bar is given to the right. The Gaussian fit of component (A) of the GBT CO(1–0) profile (Figure 2) is shown by the dotted line and has been normalized to the peak of the Hanning-smoothed CO(3–2) spectrum represented by the diamonds.

a distinct component showing much lower CO excitation than that found from L1 and L2SW. A natural question is: where is the molecular gas associated with velocity component (A) located?

Deep sub-arcsec CO(3–2) imaging with ALMA has helped to explain the nature of component (A). Figure 5 shows the ALMA CO(3–2) channel maps smoothed over $300\,\mathrm{km\,s^{-1}}$. The three panels corresponding to center velocities +40, −260, and $-560\,\mathrm{km\,s^{-1}}$ cover the velocity range associated with component (B), while the panel centered on $+340\,\mathrm{km\,s^{-1}}$ corresponds to component (A). The $+340\,\mathrm{km\,s^{-1}}$ panel shows a new extended component of molecular gas (designated "W1") that extends several arcsec westward from L2SW and L1. The CO(3–2) spectrum for W1 has a velocity and line width that closely matches component (A) of the GBT CO(1–0) profile (Figure 6). The total linear extent of the molecular gas for SMM02399 (L2SW+L1+W1) corresponds to $3\farcs2$ (25 kpc) in the source-frame, after correcting for lensing, which shears the source emission roughly along the long axis of the observed CO emission.

In addition to uncovering a new extended component of molecular gas (W1), the ALMA CO(3–2) data show velocity gradients consistent with rotation for both L2SW and L1. By comparing panels +40, −260, and $-560\,\mathrm{km\,s^{-1}}$, an obvious velocity gradient across L2SW is observed with a position angle of about 105° on the sky. The data also show evidence for a velocity gradient across L1. A straightforward interpretation of these observations is that both L2SW and L1 are associated with separate disks of molecular gas undergoing starburst activity. These data will be analyzed and modeled in detail in a future paper. No molecular gas was detected from the L2 or L1N optical components.

The CO(3–2) emission peaks on the starburst region of L2SW, and this region is more than three times brighter in CO (3–2) than the AGN component L1 (Figure 7). The CO(3–2) spectrum from only the central L2SW and L1 regions does not show the excess CO emission seen at positive velocities associated with component (A). However, using an aperture that also contains the new faint western feature W1, the total CO(3–2) spectrum resembles the GBT CO(1–0) profile (Figure 7).

3.3. CO Excitation

The two velocity components of the GBT CO(1–0) profile show very different CO excitation (Table 4), as highlighted by Figure 4. With the single-dish GBT CO(1–0) data, we cannot fully disentangle the CO excitation spatially for the system, but we can measure the excitation for the two velocity components. Velocity component (B) is comprised of L2SW and L1, while the emission from velocity component (A) comes from L2SW,

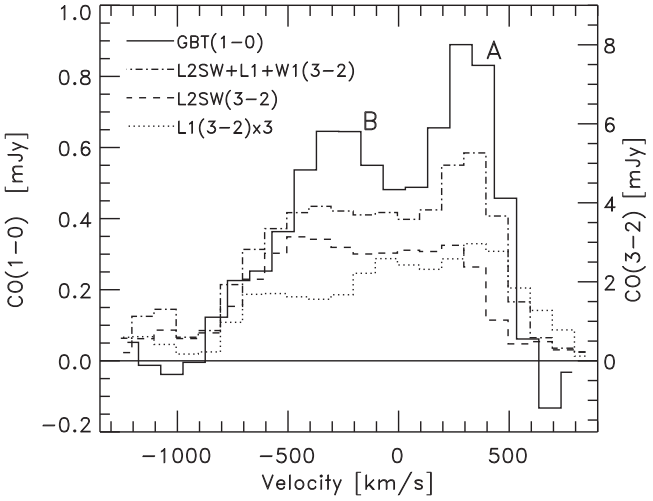

Figure 7. Total ALMA CO(3–2) spectrum, shown by the dashed–dotted line labeled as L2SW+L1+W1(3–2), compared to the GBT CO(1–0) spectrum (solid line). The ALMA CO(3–2) spectra for L2SW and L1 are shown as dashed and dotted lines, respectively. All spectra have channels of 100 km s^{-1} and have been Hanning-smoothed. The spectrum for L1 has been scaled up by a factor of three for comparison purposes. The CO(3–2) axis has been scaled to $r_{31} = 1$ for comparison with CO(1–0).

Table 4
CO Brightness Temperature Ratios

	r_{31}	r_{71}
(A)	0.58 ± 0.11	<0.009
(B)	0.66 ± 0.13	0.095 ± 0.017

Note. The observed CO brightness temperature ratios for velocity components (A) and (B), where $r_{ij} = T_b(i - [i-1])/T_b(j - [j-1])$. The upper limit represents 3σ, and the errors include the flux calibration uncertainty. The ratios are based on the measured peaks of the two components.

L1, and the new component, W1. To study the CO excitation of velocity components (A) and (B), we used the radiative transfer code RADEX (van der Tak et al. 2007). We adopted typical CO abundance ratios and velocity gradients used in Large-Velocity-Gradient modeling for Galactic molecular gas (e.g., de Jong et al. 1975) to compute the predicted CO spectral-line energy distributions for a range of physical properties (Figure 8). Although we have data for only three CO transitions, the observed line ratios rule out significant parameter space. The relatively high CO(3–2)/CO(1–0) brightness temperature ratios of $r_{31} \gtrsim 0.6$ imply densities larger than 10^3 cm^{-3}, while the ratios of $r_{71} < 0.1$ imply densities lower than 10^5 cm^{-3}.

The modeling with RADEX and the observed r_{71} ratio suggests that the properties for component (B) are consistent with local starbursts with densities of the order of 10^4 cm^{-3} (Kamenetzky et al. 2014; Zhang et al. 2014; Mashian et al. 2015) and temperatures of 40–50 K, which agrees with the inferred single-component dust temperature of 41 ± 1 K derived from *Herschel* photometry measurements (Magnelli et al. 2012). In contrast, component (A) shows CO ratios consistent with lower temperatures and densities that are in rough agreement with values found for molecular cloud complexes within the Milky Way (Fixsen et al. 1999; Friesen et al. 2017).

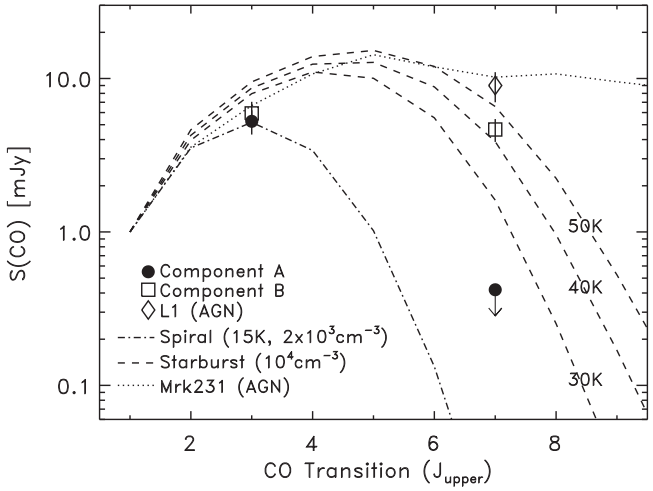

Figure 8. The modeled CO spectral-line energy distribution normalized to CO (1–0) for a spiral galaxy with an excitation temperature of 15 K and density of 2×10^3 cm^{-3} is shown as the dashed–dotted line, while models for starbursts with a density of 10^4 cm^{-3} and temperatures of 30, 40, and 50 K are shown as dashed lines. The X-ray-dominated AGN source Mrk 231 (van der Werf et al. 2010) is shown by the dotted line. The observed measurements for velocity components (A) and (B) are shown by the solid circles and open squares, respectively. Component (A) can be fitted by a spiral galaxy model, while component (B) shows higher CO excitation consistent with a starburst. The diamond symbol represents the estimated ratio for the AGN component L1.

The r_{73} ratio associated with L1 is three times larger than that observed for L2SW, which implies different CO excitation in L1 and L2SW. Assuming the same r_{31} ratio for L1 and L2SW as derived for velocity component (B), then the implied CO(7–6) to CO(1–0) flux density ratio for L1 is estimated to be 9 ± 2 (diamond symbol in Figure 8). This value is arguably a lower limit if r_{31} is higher for L1 than L2SW. The inferred high r_{71} ratio for L1 is consistent with high excitation associated with X-ray emission from the AGN, as seen in some local ultraluminous infrared galaxies (ULIRGs; van der Werf et al. 2010; Mashian et al. 2015).

4. Discussion

4.1. Total Amount of Molecular Gas

The single-dish CO(1–0) measurements from the GBT provide the best constraints on the total amount of molecular gas in the system. Since the two velocity components show different CO excitation, they may have different CO-to-H_2 conversion factors.[7] For the starburst component (B), we adopt the standard ULIRG value of $\alpha_{CO} = 0.8\,M_\odot$ (K km s^{-1} pc^2)$^{-1}$ (Downes & Solomon 1998). This value could significantly underestimate the amount of gas arising from a high density phase of the interstellar medium as discussed by Papadopoulos et al. (2012), but the observed r_{71} ratio for SMM02399 argues against most of the molecular gas existing in very dense regions (Section 3.3). The CO-to-H_2 conversion factor for component (A) is arguably even more uncertain, but it is expected to be higher than the value for the starburst component. We adopt the Galactic value of $4.3\,M_\odot$ (K km s^{-1} pc^2)$^{-1}$ (Bolatto et al. 2013) for component (A) due to its lower CO excitation. If the molecular gas in component

[7] The molecular gas mass (M[H_2]) derived by the CO-to-H_2 conversion factor includes He.

(A) has low metallicity, the CO-to-H_2 conversion factor could be much higher, as found for metal-poor galaxies in the local universe (Rubio et al. 1993; Wilson 1995; Israel 1997; Leroy et al. 2011; Schruba et al. 2012; Amorín et al. 2016).

Assuming the ULIRG CO-to-H_2 conversion factor for component (B) and the Galactic conversion factor for component (A), SMM02399 has a total molecular gas mass of $M(H_2) = (2.3 \pm 0.3) \times 10^{11} (\alpha/2.1)\, M_\odot$, with an effective single-value CO-to-H_2 conversion factor of $\alpha_{CO} = 2.1\, M_\odot$ $(K\,km\,s^{-1}\,pc^2)^{-1}$. Velocity component (A) is responsible for about 40% of the total CO(1–0) luminosity, but contains about 75% of the total molecular gas mass based on the adopted conversion factors.

4.2. The Nature of W1

The molecular gas mass associated with W1 that is spatially offset from the central L2SW/L1 regions is estimated to be $M(H_2) = (6.6 \pm 1.2) \times 10^{10} (\alpha/4.3)\, M_\odot$, based on the fractional CO(3–2) emission associated with this component, assuming the same r_{31} ratio for all gas in component (A), and using the adopted CO-to-H_2 conversion factor. This represents about 30% of the total molecular gas mass in the system. A rough estimate for the dynamical mass can be derived by assuming the gas in W1 is bound and that the kinematics are dominated by isotropic turbulent motions. With these assumptions, the dynamical mass is $M_{dyn} = 2.3 \times 10^5 R_{kpc} (3\sigma_v^2)\, M_\odot$, where σ_v is the velocity dispersion in units of $km\,s^{-1}$. W1 extends 13 kpc from L1 ($R_{kpc} = 6.5$), and using the measured FWHM of component (A), the dynamical mass of W1 is $M_{dyn} = (5.5 \pm 1.4) \times 10^{10}\ M_\odot$. These results are consistent with the mass of W1 being dominated by molecular gas with a gas fraction near unity ($M(H_2)/M_{dyn} = 1.2 \pm 0.4$ $[\alpha/4.3] \approx 1$). There is no detected stellar component for W1 (Figure 1). Aguirre et al. (2013) derived the stellar masses of the optical components of SMM02399 based on their colors and stellar population models. Using these results and assuming similar stellar populations for W1 as derived for the nearby starburst region L2SW/L1sb, the 3σ upper limit on the stellar mass for W1 is $M_* < 0.4 \times 10^{10} M_\odot$ based on the noise level measured within the publicly available deep 1.6 μm Frontier Fields image (Lotz et al. 2017). The large molecular gas to stellar mass ratio of $M(H_2)/M_* > 16$ for W1 is more than a factor of 100 larger than that found for normal local galaxies and 10 times larger than that derived for molecular-rich galaxies at high redshift (e.g., Popping et al. 2015, and references therein).

The exact nature of W1 is unclear. We discuss three possible explanations: (1) merger remnant, (2) outflow from the AGN, and (3) inflowing gas.

The first explanation that W1 is a tidal remnant is arguably the most natural explanation given the observed kinematics and source morphology. The kinematics of W1 appear to connect fairly smoothly along the major axis of the massive molecular disk associated with L2SW. However, most of the gas associated with mergers is expected to be concentrated in the central regions and not in tidal debris. The numerical simulations of Barnes (2002) show that the central regions of gas-rich mergers are expected to contain 85%–95% of the gas mass, while the surrounding loops and tidal tails are expected to contain only 5%–15% of the gas mass. The derived 30% gas mass fraction for W1 is higher than these predictions, but SMM02399 could still be in the early stages of the merger event whereby much of the mass of W1 may fall back into the central regions. Also, the details of the merger orientation and kinematics are important. If L2SW and L1 are undergoing a prograde interaction within the same plane, we could expect a tidal arm feature at the position of W1 that is amplified based on the modeling of Oh et al. (2015), which may explain the higher than expected mass fraction for W1.

A second possible explanation is that W1 is due to a massive molecular outflow associated with the powerful AGN. SMM02399 has a significantly lower infrared-to-radio luminosity ratio than that found for starbursts, implying the importance of the AGN for the radio emission (Frayer et al. 1998). Also, the radio emission extends over 7″ in the east–west direction between L1 and L2/L2SW (Ivison et al. 2010) and is aligned with the direction of the W1 emission. The excess radio emission and its alignment along the direction of the W1 emission may suggest a physical connection between the AGN and the W1 molecular gas. The observed GBT CO(1–0) profile also appears very similar to predicted single-dish CO profiles from gas-rich merger models that include AGN feedback with outflows (Narayanan et al. 2006). These simulations predict a narrow velocity-width CO component due to the outflow that is offset in velocity from the underlying broad velocity component arising from the central star-forming regions. The narrow CO line widths of these modeled outflows appear consistent with slow-moving molecular outflows as seen in local starbursts, such as M82 (Walter et al. 2002), instead of the fast-moving outflows seen locally for powerful AGNs that show very broad CO velocity profiles (e.g., Mrk 231, Feruglio et al. 2010).

In the merger simulations of Narayanan et al. (2006, 2008), the typical outflow mass is predicted to represent 5%–15% of the total molecular gas mass, which is less than the 30% mass fraction estimated for W1. However, other models have predicted higher mass fractions for AGN-dominated outflows in high-redshift galaxies in rough agreement with W1 (e.g., Biernacki & Teyssier 2018). If W1 is an outflow, the power associated with the kinetic energy of the outflow is about $9 \times 10^{10} L_\odot$, which is about 1% of the bolometric luminosity of the system and well within the realm of possibility.

A third explanation for W1 is that this molecular gas is inflowing material associated with the formation of the galaxy. Cosmological models for the formation of SMGs predict massive gaseous inflows and clumps of gas infalling into the central regions that build up the mass of the galaxy over time (Davé et al. 2010; Narayanan et al. 2015). The early inflowing material is expected to be metal-poor, and if so, then the mass of molecular gas could be 10 times larger than that estimated in Section 4.1 due to a higher CO-to-H_2 conversion factor. For metal-poor gas, CO is not a good tracer of the total molecular gas mass, due to the photodissociation of CO molecules from a lack of shielding (Wolfire et al. 2010). If the bulk of the molecular gas in SMM02399 is metal-poor infalling material, then we would expect to find strong atomic [C I] emission in comparison to CO. The lack of a strong enhancement of [C I] emission for SMM02399 (Walter et al. 2011) argues strongly against the scenario of W1 resulting from metal-poor inflowing gas. However, W1 may be inflowing metal-enriched gas. Recent observations have suggested the existence of metal-enriched gas within the molecular circumgalactic medium of the $z = 2.2$ Spiderweb (Emonts et al. 2018).

5. Concluding Remarks

In this paper, we present GBT and ALMA CO observations of the $z = 2.8$ SMG SMM02399. The GBT observations uncovered a component of excess CO(1–0) emission. This component has the same velocity and line width as a new faint structure (W1) imaged in CO(3–2) extending 13 kpc westward from the AGN. The exact nature of W1 is currently unclear, but it is estimated to contain about 30% of the total molecular gas in the system.

The results for SMM02399 highlight the potential contribution that single-dish observations can have for studying molecular emission on large spatial scales for high-redshift galaxies. In general, most high-redshift CO interferometric observations are limited to detecting only the bright central cores of young galaxies. The amount of molecular gas on large spatial scales is currently unclear, although models predict a significant amount of gas, on the scale of galaxy halos (∼100 kpc), for galaxies in their formative phases (Narayanan et al. 2015), and recent observations support these models by detecting molecular gas on large scales in the Spiderweb system (Emonts et al. 2016, 2018). Single-dish observations of high-redshift CO(1–0), in particular with the GBT (Hainline et al. 2006; Swinbank et al. 2010; Frayer et al. 2011; Harris et al. 2012; Harrington et al. 2018), can test for the presence of excess CO emission and measure the total molecular gas reservoirs of young systems.

We thank our colleagues at the Green Bank Observatory, who have made these observations possible. We greatly appreciate the staff at the North American ALMA Science Center, who calibrated the raw ALMA visibilities. The Green Bank Observatory and the National Radio Astronomy Observatory are facilities of the National Science Foundation operated under cooperative agreements by Associated Universities, Inc.

This paper makes use of the following ALMA data: ADS/JAO.ALMA #2013.1.00403.S, ADS/JAO.ALMA #2015.1.00302.S. ALMA is a partnership of ESO (representing its member states), NSF (USA) and NINS (Japan), together with NRC (Canada), *MOST* and ASIAA (Taiwan), and KASI (Republic of Korea), in cooperation with the Republic of Chile. The Joint ALMA Observatory is operated by ESO, AUI/NRAO, and NAOJ. The optical image is based on observations obtained with the NASA/ESA *Hubble Space Telescope*, retrieved from the Mikulski Archive for Space Telescopes (MAST) at the Space Telescope Science Institute (STScI). STScI is operated by the Association of Universities for Research in Astronomy, Inc. under NASA contract NAS 5-26555. R.J.I. acknowledges ERC funding in the form of Advance Grant COSMICISM (321302). I.R.S. acknowledges support from the ERC Advance Grant DUSTYGAL (321334), a Royal Society/Wolfson Award, and STFC(ST/P000541/1).

Facilities: GBT, ALMA.

Software: RADEX (van der Tak et al. 2007), GBTIDL (Marganian et al. 2006), CASA (McMullin et al. 2007).

ORCID iDs

David T. Frayer https://orcid.org/0000-0003-1924-1122
R. J. Ivison https://orcid.org/0000-0001-5118-1313
Ian Smail https://orcid.org/0000-0003-3037-257X
Andrew W. Blain https://orcid.org/0000-0001-7489-5167
Paul Vanden Bout https://orcid.org/0000-0003-3304-3974

References

Aguirre, P., Baker, A. J., Menanteau, F., Lutz, D., & Tacconi, L. J. 2013, ApJ, 768, 164
Amorín, R., Muñoz-Tuñón, C., Aguerri, J. A. L., & Planesas, P. 2016, A&A, 588, A23
Barger, A. J., Cowie, L. L., Sanders, D. B., et al. 1998, Natur, 394, 248
Barnes, J. E. 2002, MNRAS, 333, 481
Bautz, M. W., Malm, M. R., Baganoff, F. K., et al. 2000, ApJ, 543, 119
Biernacki, P., & Teyssier, R. 2018, MNRAS, 475, 5688
Blain, A. W., Smail, I., Ivison, R. J., Kneib, J.-P., & Frayer, D. T. 2002, PhR, 369, 111
Bolatto, A. D., Wolfire, M., & Leroy, A. K. 2013, ARA&A, 51, 207
Casey, C. M., Narayanan, D., & Cooray, A. 2014, PhR, 541, 45
Davé, R., Finlator, K., Oppenheimer, B. D., et al. 2010, MNRAS, 404, 1355
de Jong, T., Dalgarno, A., & Chu, S.-I. 1975, ApJ, 199, 69
Downes, D., & Solomon, P. M. 1998, ApJ, 507, 615
Emonts, B. H. C., Lehnert, M. D., Dannerbauer, H., et al. 2018, MNRAS, 477, L60
Emonts, B. H. C., Lehnert, M. D., Villar-Martín, M., et al. 2016, Sci, 354, 1128
Ferkinhoff, C., Brisbin, D., Nikola, T., et al. 2011, ApJL, 740, L29
Ferkinhoff, C., Brisbin, D., Nikola, T., et al. 2015, ApJ, 806, 260
Ferkinhoff, C., Hailey-Dunsheath, S., Nikola, T., et al. 2010, ApJL, 714, L147
Feruglio, C., Maiolino, R., Piconcelli, E., et al. 2010, A&A, 518, L155
Fixsen, D. J., Bennett, C. L., & Mather, J. C. 1999, ApJ, 526, 207
Frayer, D. T., Harris, A. I., Baker, A. J., et al. 2011, ApJL, 726, L22
Frayer, D. T., Ivison, R. J., Scoville, N. Z., et al. 1998, ApJL, 506, L7
Friesen, R. K., Pineda, J. E., Rosolowsky, E., et al. 2017, ApJ, 843, 63
Genzel, R., Baker, A. J., Tacconi, L. J., et al. 2003, ApJ, 584, 633
Hainline, L. J., Blain, A. W., Greve, T. R., et al. 2006, ApJ, 650, 614
Harrington, K. C., Yun, M. S., Magnelli, B., et al. 2018, MNRAS, 474, 3866
Harris, A. I., Baker, A. J., Frayer, D. T., et al. 2012, ApJ, 752, 152
Hughes, D. H., Serjeant, S., Dunlop, J., et al. 1998, Natur, 394, 241
Israel, F. P. 1997, A&A, 328, 471
Ivison, R. J., Smail, I., Le Borgne, J.-F., et al. 1998, ApJ, 298, 583
Ivison, R. J., Smail, I., Papadopoulos, P. P., et al. 2010, MNRAS, 404, 198
Kamenetzky, J., Rangwala, N., Glenn, J., Maloney, P. R., & Conley, A. 2014, ApJ, 795, 174
Leroy, A. K., Bolatto, A., Gordon, K., et al. 2011, ApJ, 737, 12
Lotz, J. M., Koekemoer, A., Coe, D., et al. 2017, ApJ, 837, 97
Lutz, D., Valiante, E., Sturm, E., et al. 2005, ApJL, 625, L83
Magnelli, B., Lutz, D., Santini, P., et al. 2012, A&A, 539, 155
Marganian, P., Garwood, R. W., Braatz, J. A., Radziwill, N. M., & Maddalena, R. J. 2006, in ASP Conf. Ser. 35, Astronomical Data Analysis Software and Systems XV, ed. C. Gabriel et al. (San Fransisco, CA: ASP), 512
Mashian, N., Sturm, E., Sternberg, A., et al. 2015, ApJ, 802, 81
McMullin, J. P., Waters, B., Schiebel, D., Young, W., & Golap, K. 2007, in ASP Conf. Ser. 376, Astronomical Data Analysis Software and Systems XVI, ed. R. Shaw, F. Hill, & D. J. Bell (San Francisco, CA: ASP), 127
Narayanan, D., Cox, T. J., Kelly, B., et al. 2008, ApJS, 175, 331
Narayanan, D., Cox, T. J., Robertson, B., et al. 2006, ApJL, 642, L107
Narayanan, D., Turk, M., Feldmann, R., et al. 2015, Natur, 525, 496
Oh, S. H., Kim, W.-T., & Lee, H. M. 2015, ApJ, 807, 73
Papadopoulos, P. P., van der Werf, P., Xilouris, E., Isaak, K. G., & Gao, Y. 2012, ApJ, 751, 10
Perley, R. A., & Butler, B. J. 2013, ApJS, 204, 19
Popping, G., Behroozi, P. S., & Peeples, M. S. 2015, MNRAS, 449, 477
Rubio, M., Lequeux, J., & Boulanger, F. 1993, A&A, 271, 9
Schruba, A., Leroy, A. K., Walter, F., et al. 2012, AJ, 143, 138
Smail, I., Ivison, R. J., & Blain, A. W. 1997, ApJL, 490, L5
Swinbank, A. M., Smail, I., Longmore, S., et al. 2010, Natur, 464, 733
Thomson, A. P., Ivison, R. J., Smail, I., et al. 2012, MNRAS, 425, 2203
Valiante, E., Lutz, D., Sturm, E., et al. 2007, ApJ, 660, 1060
van der Tak, F. F. S., Black, J. H., Schöier, F. L., Jansen, D. J., & van Dishoeck, E. F. 2007, A&A, 468, 627
van der Werf, P. P., Isaak, K. G., Meijerink, R., et al. 2010, A&A, 518, L42
Vernet, J., & Cimatti, A. 2001, A&A, 380, 409
Walter, F., Weiß, A., Downes, D., Decaril, R., & Henkel, C. 2011, ApJ, 730, 18
Walter, F., Weiß, A., & Scoville, N. 2002, ApJL, 580, L21
Wilson, C. D. 1995, ApJL, 448, L97
Wolfire, M. G., Hollenbach, D., & McKee, C. F. 2010, ApJ, 716, 1191
Zhang, Z.-Y., Henkel, C., Gao, Y., et al. 2014, A&A, 568, 122